



In-situ growth of amorphous MnO₂ on C-decorated Fe-based geopolymer sphere with rich structure defects for efficient solar light-induced photo-thermal-Fenton reaction

Xiunan Cai, Meifei Chen, Chuanyi Zhong, Jiayue Lu, Yanmei Huang, Yanjuan Zhang^{*}, Tao Gan, Huayu Hu, Zuqiang Huang^{*}

School of Chemistry and Chemical Engineering, Guangxi University, Nanning 530004, China

ARTICLE INFO

Keywords:

Amorphous MnO₂
structure defects
Fe-based geopolymer
photo-thermal-Fenton
tetracycline hydrochloride

ABSTRACT

Crystalline MnO₂ exhibits excellent photo-thermal conversion and adjustability of valence states properties, but the weak near-infrared light absorption, poor charge transportation and utilization limit its environmental applications. Herein, a novel Na-doped amorphous MnO₂/C-decorated Fe-based geopolymer sphere (A-MnO₂/C-FeGS) with rich structure vacancies was constructed by ion exchange anchoring strategy and used to degrade tetracycline hydrochloride (TC) in solar light-induced photo-thermal-Fenton process. Manganese residue (MR), an industrial solid waste, was used as the source of Fe and Si. A-MnO₂/C-FeGS exhibited excellent catalytic performance with TC removal of 98.2% within 30 min, being about 4.5 and 3.3 times faster than crystalline MnO₂ and C-FeGS, respectively. The improved photocatalytic activity was attributed to that rich oxygen vacancies could provide more catalytic active sites and accelerate Fe³⁺/Fe²⁺ and Mn⁴⁺/(Mn²⁺+Mn³⁺) conversion for more ·OH generation. Moreover, Na-doped amorphous MnO₂ and C decoration synergistically contributed to high photo-thermal conversion rate, which could in-situ heat the catalyst and induce the activation of H₂O₂. This promoted the activation of the surface lattice oxygen and accelerated the secondary transition and utilization of the thermal electrons captured by the defect sites. This work provides a novel strategy for the development of highly reactive catalysts and valorization of MR in the field of environmental remediation.

1. Introduction

The abuse and random discharge of persistent pollutants (dyes, antibiotics, pesticides, etc.) are posing a potential threat to human health and ecological environment [1,2]. Among them, antibiotics are widely used in clinical medicine and animal husbandry. Tetracycline hydrochloride (TC), one of the most stubborn antibiotics, has been widely used in many countries as therapeutic medicine, especially in the livestock husbandry to treat infections. Thus, TC is inevitably discharged into aquatic ecosystem via biological metabolism [3,4]. Moreover, owing to the characteristics of good water solubility and poor biodegradability, TC is frequently detected in water bodies, leading to a serious threat to aquatic life and human beings without effective treatment [4]. Recently, heterogeneous photo-Fenton reaction is demonstrated as a promising technology to efficiently treat persistent organic pollutants in wastewater due to the synergistic effect of photocatalytic and Fenton reaction, which could accelerate the regeneration of Mⁿ⁺/M⁽ⁿ⁺¹⁾⁺ (M represents

the transition metal atoms), thus promoting the production of hydroxyl radicals (·OH) [5-7]. A series of Mn-based [8], Fe-based [9], and Cu-based [5,10] catalysts with adjustable valences and good visible light absorption capacity have been developed in photo-Fenton system [11]. Manganese dioxide (MnO₂), a narrow bandgap (~1.7 eV) transition metal oxide, has been widely used for Fenton catalysis [12], thermal catalysis [13,14], electrocatalysis [15,16], and photocatalysis [17] on account of its cost effectiveness, natural abundance, excellent adjustability of valence states, and controllability of crystal structure [18]. Among them, the transformation between Mn⁴⁺ and Mn³⁺/Mn²⁺ for promoting the formation of oxygen vacancies and the high efficiency of solar-driven photo-thermal catalysis are the most important [19]. Different crystal types and surface structures of MnO₂ show great differences in surface oxygen vacancy content and catalytic performance [20]. However, the crystalline MnO₂ polymorphs always suffer from the problems of low catalytic activity, poor near-infrared light adsorption, and inefficient charge transportation and utilization. In contrast,

^{*} Corresponding authors.

E-mail addresses: zhangyj@gxu.edu.cn (Y. Zhang), huangzq@gxu.edu.cn (Z. Huang).

<https://doi.org/10.1016/j.cej.2022.137857>

Received 21 April 2022; Received in revised form 18 June 2022; Accepted 28 June 2022

Available online 30 June 2022

1385-8947/© 2022 Elsevier B.V. All rights reserved.

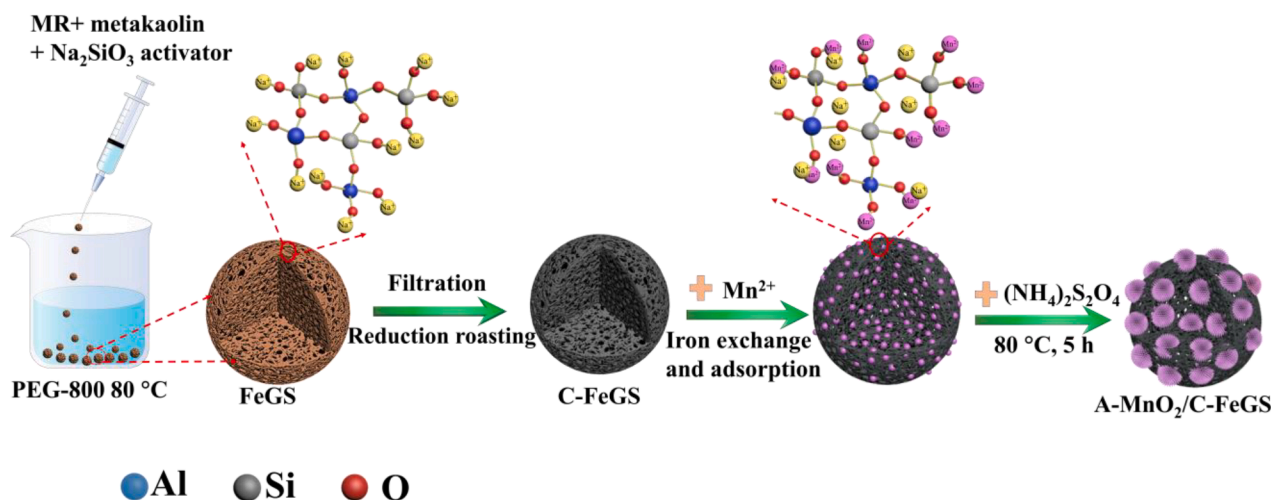


Fig. 1. Schematic diagram of the synthetic process of A-MnO₂/C-FeGS.

amorphous MnO₂ has more flexible structures and abundant oxygen vacancies owing to its short-range ordered and long-range disordered structures, which can provide abundant active sites [15,21]. Specially, amorphous MnO₂ has been successfully prepared by in-situ redox reaction [22], redox reaction in the saturated sodium chloride solution [23], and hydrothermal method [15], and been widely used in the field of electrocatalysis [15,23]. In this regard, it is reasonable to assume that amorphous structure could improve the photocatalytic performance of MnO₂. Thus, the construction of amorphous MnO₂-based catalysts with high photocatalytic activity through a facile way is challengeable and significant.

In addition, thermally-assisted technology is considered as an effective strategy to strengthen photocatalytic performance [24,25], and the separation efficiency of photogenerated electrons and holes (e⁻-h⁺) could be enhanced when receiving thermal activation [26]. Solar energy is clean and free, and this largest available energy source has caused wide research [27]. Unfortunately, the strong absorption of MnO₂ on solar light mainly occurs in the ultraviolet (UV), visible (Vis) and a small part of near-infrared (NIR) region [28], which accounts for nearly half of solar energy could not be fully utilized [27]. Coupling carbon-based materials (rGO [14,29], polydopamine [17] and bilayer paper [30]) with transition metal has been verified to greatly extend the light adsorption and increase the photo-thermal conversion capacity. Besides, Fe-based materials are widely used to compound with MnO₂ to overcome its shortcomings of lower reactivity and difficulty in recovery [31-33]. Nevertheless, current researches are focusing on the effect of Fe-Mn interaction on the activation of H₂O₂ and the magnetic recovery performance, ignoring the strengthening effect of photo-thermal conversion characteristics of MnO₂ on photo-Fenton system. Therefore, it is highly desirable to construct an amorphous MnO₂-based photo-thermal-Fenton catalyst with favorable structure, special morphology, and strong light absorption capacity through a simple and green method.

Porous geopolymer as one of the geopolymer-based porous materials, synthesized by mixing alkali-activator with metakaolin or industrial waste (blast furnace slag [34], fly ash [35], steel slag [36], or manganese residue [37]), has been widely used in adsorption [38], catalysis [39], filtration and separation owing to its good permeability and low cost. Manganese residue (MR) is produced in the production process of manganese sulfate with pyrolusite and pyrite as materials in sulfuric acid solution. As the containing of abundant Fe and Si, MR has been successfully used to prepare Fe-based catalysts [40-42]. On this basis, MR can be applied to prepare porous geopolymer for using as the support of MnO₂. Furthermore, C can be combined into the geopolymer to prepare C-decorated geopolymer for improving the properties of MnO₂. Based on above-mentioned issues, the C-decorated geopolymer

used for supporting MnO₂ may provide the following advantages: (1) Mn²⁺ can be quickly adsorbed on the support owing to the tetrahedron [SiO₄]⁴⁻ and [AlO₄]⁵⁻ in geopolymer and the rich alkali metals in solution can effectively regulate the crystal growth of MnO₂; (2) MnO₂ can cooperate with C to enhance light absorption and accelerate electron transport; (3) the pore structure inner geopolymer provides more attachment sites for the growth of MnO₂; (4) MnO₂ coupling with the Fe oxide in geopolymers can synergistically boost the activation of H₂O₂. Therefore, it is feasible and significant to construct a C-decorated Fe-based geopolymer sphere-supported amorphous MnO₂ photocatalyst with favorable structure and special morphology to fully utilize solar energy.

In this work, a novel amorphous MnO₂/C-decorated Fe-based geopolymer sphere (A-MnO₂/C-FeGS) was fabricated and used as a highly active photocatalyst for solar light-induced photo-thermal-Fenton reaction. C-FeGS was prepared by a solidification/pyrolysis method with MR as the source of Fe and Si, H₂O₂ as foaming agent, sodium dodecyl sulfate as foaming stabilizer, and PEG-800 as curing agent and carbon source. Subsequently, Na-doped amorphous MnO₂ was in-situ grown on C-FeGS to prepared A-MnO₂/C-FeGS via ion exchange anchoring strategy and persulfate oxidation method, which was used as a highly active photocatalyst for effectively degrading TC in solar light-induced photo-thermal-Fenton process. Systematic characterizations were performed to measure the structure, morphology, chemical compositions, and surface states of the catalyst. The photo-thermal conversion efficiency, activation of H₂O₂, separation of photoelectron-hole, and utilization rate of thermal electrons in photo-Fenton system referring to the structural characteristics of the catalyst were investigated in depth. Furthermore, potential catalytic mechanism and possible degradation pathways of TC over A-MnO₂/C-FeGS were proposed. The present work can provide a promising strategy to develop highly active MnO₂-based catalysts for efficient photo-Fenton reaction.

2. Experimental section

2.1. Materials

Water glass [$n(\text{SiO}_2)/n(\text{Na}_2\text{O}) = 3.3$] was provided by Chunxu Chemical (Nanning, China). MR was pre-roasted at 600 °C for 6 h, which was mainly composed of Fe₂O₃ and SiO₂, and the chemical compositions are listed in Table S1 (Supplementary Material). Kaolin was pre-roasted at 800 °C for 2 h to obtain the metakaolin. PEG-800, sodium hydroxide (NaOH), hydrogen peroxide (H₂O₂), sodium dodecyl sulfate (K12), manganese sulfate monohydrate (MnSO₄·H₂O), and ammonium persulfate ((NH₄)₂S₂O₈) were purchased from Damao Chemical Regent

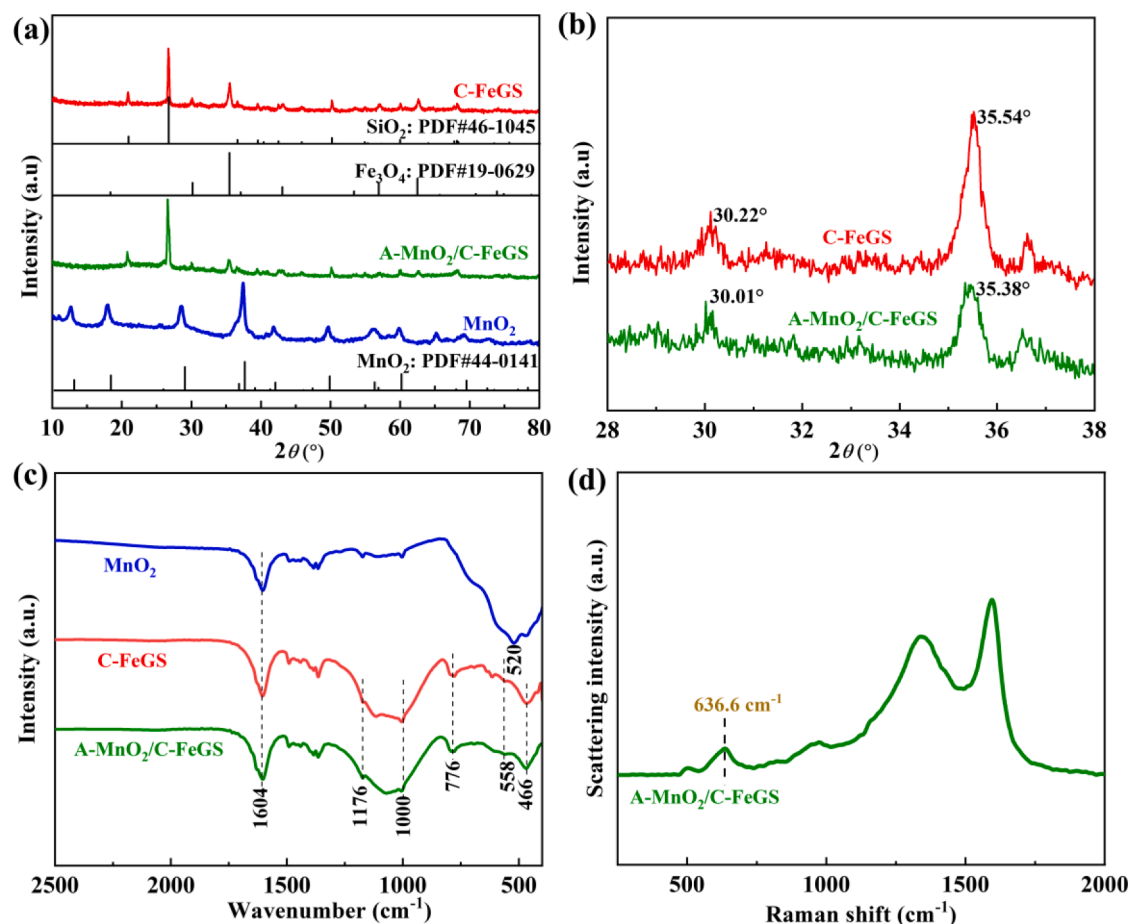


Fig. 2. (a) XRD patterns, (b) enlarge part ranging from 28° to 38°, and (c) FTIR spectra of C-FeGS, MnO₂, and A-MnO₂/C-FeGS; (d) Raman spectrum of A-MnO₂/C-FeGS.

Company (Tianjin, China). Tetracycline hydrochloride (TC), methylene blue (MB), methyl orange (MO), rhodamine B (RB), and ciprofloxacin (CIP) were provided by Aladdin Industrial Corporation (Shanghai, China).

2.2. Preparation of photocatalysts

2.2.1. Preparation of C-FeGS

C-FeGS was prepared by a solidification pyrolysis method. Typically, 22.14 g of NaOH was dissolved in 200 g water glass with continuous stirring for 24 h to obtain modified water glass. The pre-roasted MR, metakaolin, modified water glass, K12, and H₂O₂ were mixed in the mass ratio of 1:0.67:1.88:0.083:0.11. Then, the slurry was dropped into PEG-800 (80 °C) using a 10 mL syringe. After solidified at 80 °C for 6 h, FeGS was formed and separated from PEG-800. Subsequently, the FeGS was calcined at 500 °C for 2 h under N₂ atmosphere to obtain C-FeGS. The C-FeGS was crushed and the particle size distribution in the range of 1–5 mm was selected.

2.2.2. Synthesis of A-MnO₂/C-FeGS

C-FeGS (3 g) was added into MnSO₄ aqueous solution (1 M, 50 mL) and stirred for 6 h at room temperature for the adsorption and ion-exchange process of Na⁺ with Mn²⁺ to obtain Mn²⁺/C-FeGS. Then, the Mn²⁺/C-FeGS (3 g) was added into (NH₄)₂S₂O₈ aqueous solution (0.4 M, 30 mL) and magnetically stirred at 80 °C for 4 h, and the mixture was filtered and washed with deionized water. The sample was dried in vacuum at 80 °C for 12 h to obtain A-MnO₂/C-FeGS composite, as shown in Fig. 1. For a comparison, bare MnO₂ was also prepared with

MnSO₄·H₂O and (NH₄)₂S₂O₈ (mol ratio of 1:1.5) as raw materials by the above method.

2.3. Characterizations

The characterization instruments and detailed parameters used in this work are provided in [Supplementary Material](#).

2.4. Photocatalytic performance test

The photo-thermal-Fenton performance of the synthesized photocatalysts was evaluated by the degradation of TC in a self-made photocatalytic system. A 500 W Xenon lamp was used as light source (solar light 320–2500 nm, NIR 800–2500 nm), and the reaction temperature was controlled using a constant temperature water bath oscillator. Typically, photocatalyst (0.08 g) was added into the TC solution (40 mL, 50 mg L⁻¹) and kept stirring in darkness for 30 min to establish adsorption-desorption equilibrium, and then 15 mM of H₂O₂ was added to the system under the irradiation of Xenon lamp. The TC concentration was determined by using a UV–Vis spectrophotometer (Beijing Purkinje, China) at the absorbance of 357 nm. The mineralization ratios of TC in the degradation process were evaluated on a multi N/C 3100 TOC analyzer (Jena, Germany). To verify the stability and adaptability of the catalysts, several cyclic degradation tests were carried out in the same conditions and the photocatalytic degradation of other four organics (MB, MO, RB, and CIP) were conducted in this system. The main reactive oxygen species in the photo-thermal-Fenton process were further identified by radical capture experiments. The different scavengers used in

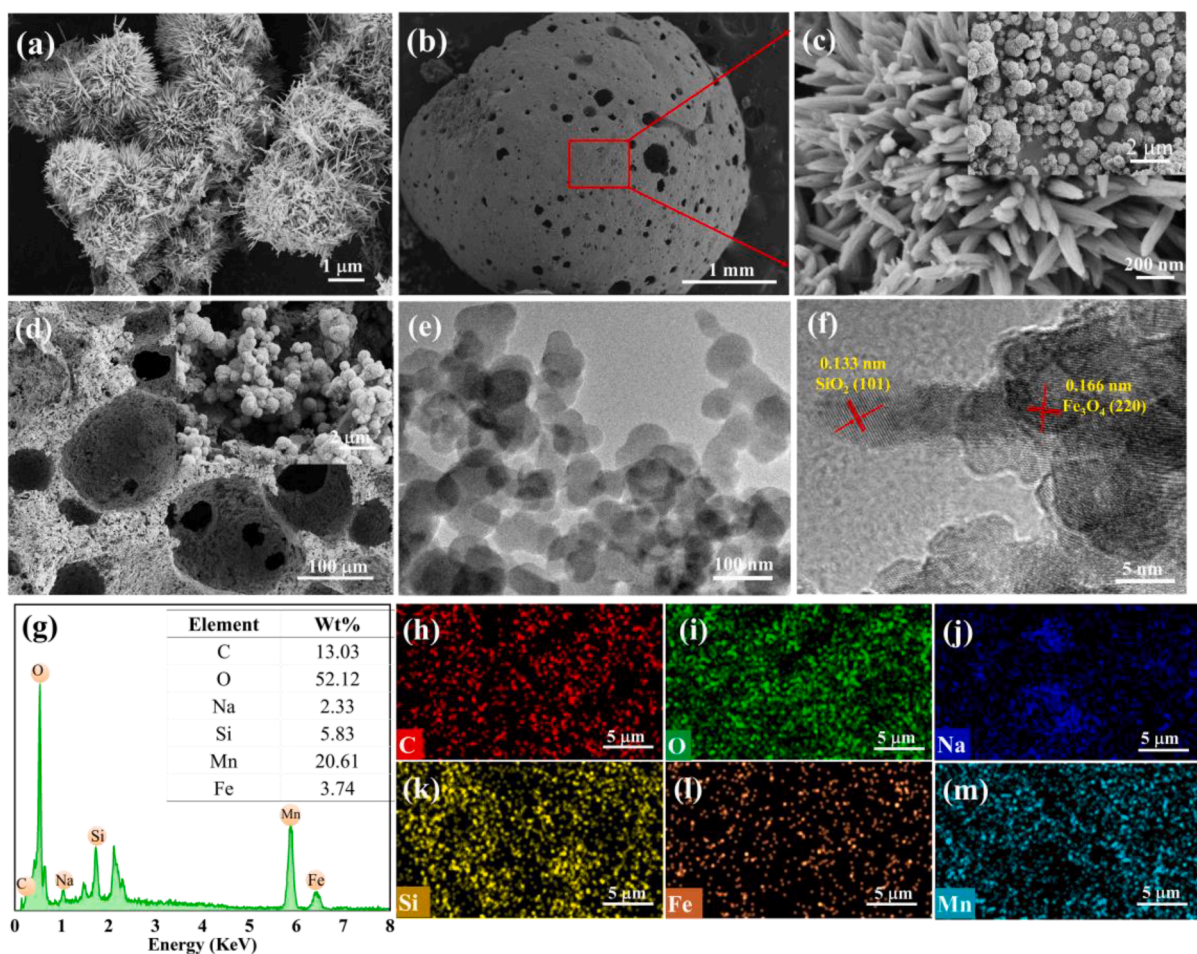


Fig. 3. SEM images of (a) MnO₂ and (b–d) inner and outside surface of A-MnO₂/C-FeGS; (e–f) HR-TEM images and (g–m) EDX analysis and element mapping of A-MnO₂/C-FeGS.

the trapping experiments were ethylenediaminetetraacetic acid disodium (EDTA-2Na, 1 mmol) for holes (h⁺), ethanol (10 mmol) for electrons (e⁻), 1,4-benzoquinone (BQ, 10 mmol) for superoxide radicals (·O₂⁻), and isopropyl alcohol (IPA, 10 mmol) for hydroxyl (·OH).

3. Results and discussions

3.1. Structural characteristics of the as-prepared catalysts

The XRD patterns of C-FeGS, MnO₂, and A-MnO₂/C-FeGS are shown in Fig. 2a. For pure MnO₂, the diffraction peaks at 12.7° (110), 18.1° (200), 28.8° (310), 37.5° (211), 41.9° (301), 49.9° (411), 56.9° (431), 60.3° (521), 65.1° (002), and 70.2° (222) could be well indexed to tetragonal α-MnO₂ phase (JCPDS No. 44-0141) [43]. As for C-FeGS, the diffraction peaks at 30.1° (220), 35.4° (311), 37.1° (222), 43.1° (400), 56.9° (511), and 62.5° (440) were ascribed to Fe₃O₄ (JCPDS 19-0629). The highest diffraction peaks appearing at 20.9°, 26.9°, 36.5°, and 50.1° were attributed to SiO₂ (JCPDS 46-1045). While after in-situ growth of A-MnO₂, no new peaks or characteristic absorption peaks of MnO₂ were observed in the XRD pattern of A-MnO₂/C-FeGS, demonstrating the amorphous structure of MnO₂. However, the peak intensities of Fe₃O₄ were significantly decreased after in-situ growth of A-MnO₂, possibly relating to the interacting of Fe₃O₄ with MnO₂. In addition, the diffraction peaks of Fe₃O₄ presented a slightly negative shift, ascribed to the replaced Mn atom with larger ion radius enlarged the crystal unit (Fig. 2b). The decreased intensity and negative shift of the diffraction peaks of Fe₃O₄ demonstrated the strong interaction of Fe–Mn in the composite. Raman spectrum (Fig. 2d) of A-MnO₂/C-FeGS shows a broad

peak located at 636.6 cm⁻¹ corresponding to the characteristic stretching vibration bands of Mn–O, indicating the existence of Mn oxide [15]. Therefore, the results of XRD and Raman analysis clearly proved that amorphous MnO₂ was successfully grown on C-FeGS to construct A-MnO₂/C-FeGS. The components of the catalysts were formed according to Eqs. 1–2:



Fig. 2c shows the functional groups of different samples identified by FTIR spectra. The peak at 1604 cm⁻¹ corresponded to the O–H flexural vibration, and the enhanced adsorption intensity in the spectra of C-FeGS and A-MnO₂/C-FeGS might be attributed to the abundant Al(OH)⁴⁻ and Si(OH)⁴⁻ in the composite [38]. The rich in –OH groups is conducive to the adsorption of Mn²⁺. The peaks located at 1000 and 776 cm⁻¹ could be ascribed to T–O–Si (T: Si or Al) asymmetric stretching vibration in geopolymer. The bands at 466 and 520 cm⁻¹ were assigned to the Fe–O and Mn–O vibration, confirming the presence of Fe and Mn oxides in the composite [7].

The morphologies and micro-structures of MnO₂ and A-MnO₂/C-FeGS were analyzed by SEM and HR-TEM, and the results are presented in Fig. 3. Bare MnO₂ exhibited a thorn ball structure with a diameter of 5–10 μm and accumulated together (Fig. 3a). A-MnO₂/C-FeGS displayed as a porous sphere with a diameter of 0.5 mm (Fig. 3b), many flower shaped microsphere of A-MnO₂ composed with nano-tentacles were anchored on the surface of C-FeGS. Notably, A-MnO₂ showed a smaller size than MnO₂, and the rich nano-tentacles is beneficial for the

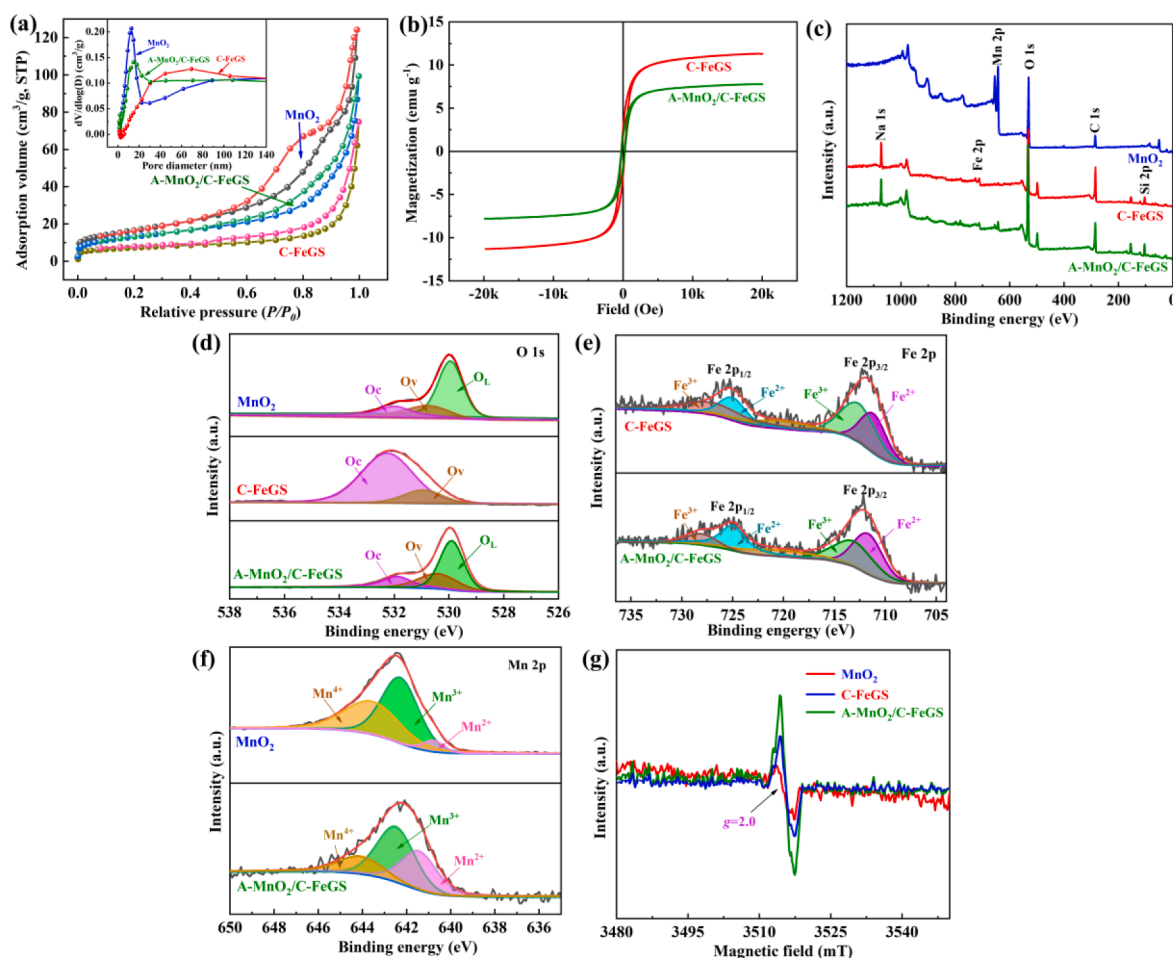


Fig. 4. (a) N_2 adsorption–desorption isotherms (inset shows BJH desorption pore size distribution plots) and (b) magnetic hysteresis curves of different samples; XPS spectra of (c) survey spectrum, (d) O 1s, (e) Fe 2p, and (f) Mn 2p of different samples; (g) EPR spectra of different samples.

adsorption of light and can provide a large specific surface area (Fig. 3c and d). The light absorbed by the composite can be refracted and reflected repeatedly between nano-tentacles and porous channels, thus greatly increasing the utilization efficiency of solar light and providing more active sites for photo-thermal-Fenton reaction. The morphology of A-MnO₂/C-FeGS demonstrated that the exchanged Na⁺ in the aqueous system had great influence on the crystal growth of MnO₂, thus significantly affecting its performance. As shown in HR-TEM images (Fig. 3e and f), metal oxides with sphere structure were uniformly mixed with C-FeGS and the clear lattice spacing of 0.133 and 0.166 nm were indexed to the (101) plane of SiO₂ and the (220) plane of Fe₃O₄, respectively. In addition, the surface element compositions of A-MnO₂/C-FeGS were determined by EDX analysis and element mapping images. As can be seen from Fig. 3g–m, Fe, Mn, C, O, Na, and Si elements coexisted in A-MnO₂/C-FeGS, indicating that the interfacial ion exchange induced in-situ growth of A-MnO₂ on C-decorated geopolymer sphere.

The N_2 adsorption–desorption isotherms and pore size distribution curves of MnO₂, C-FeGS, and A-MnO₂/C-FeGS are shown in Fig. 4a and Table S2. These three catalysts exhibited the characteristics of type IV isothermal curves with a H₃ hysteresis loop [7]. MnO₂ showed the largest surface area of 59.39 m² g⁻¹ and a pore volume of 0.1961 cm³ g⁻¹. While the BET surface area obviously increased from 18.77 to 35.29 m² g⁻¹ with the pore volume increased from 0.099 to 0.1485 cm³ g⁻¹ after in-situ growth of A-MnO₂. The increased BET surface area and pore volume could be ascribed to the abundant microspheres composed with nano-tentacles anchored on the surface of the C-FeGS, which could provide more active sites for the reaction. VSM analysis was applied to

investigate the magnetic behavior of the samples (Fig. 4b). MnO₂ was hardly to be separated from water due to its nonmagnetic properties, while the C-FeGS and A-MnO₂/C-FeGS with saturation magnetization (M_s) values of 11.3 and 8.1 emu g⁻¹ could be easily recovered from the aqueous solution by a magnet.

The XPS survey was employed to further analyze the surface element compositions and the vacancies position of MnO₂, C-FeGS, and A-MnO₂/C-FeGS. As illustrated in Fig. 4c, the main elements in different samples were confirmed by the full survey scan of XPS. Fig. 4d shows that the O 1s spectra could be fitted to three peaks of chemisorbed or dissociated oxygen species (O_C, 531.8 eV), oxygen vacancy (O_V, 530.2 eV), and lattice oxygen (O_L, 529.8 eV) [20,44]. The content of oxygen vacancy was increased from 27.5% to 38.6% after in-situ growth of A-MnO₂ on the surface of C-FeGS, attributed to that the Mn ions in the lattice were replaced by Na⁺, thus leaving more oxygen vacancies. The rich oxygen vacancies on the surface of the catalysts are beneficial for the activation of oxygen, improving the charge separation and providing more active sites. Moreover, the oxygen vacancy defect was further estimated by EPR analysis. Fig. 4g shows that all samples presented symmetrical EPR signals at $g = 2.0$, demonstrating the exit of unpaired electrons trapped by oxygen vacancies in the catalysts [29]. Notably, the EPR signal intensity of A-MnO₂/C-FeGS was higher than that of MnO₂ and C-FeGS, confirming the increased content of oxygen vacancies in A-MnO₂/C-FeGS, which is good consistent with the XPS analysis. In addition, the rich content of O_C (72.6%) in C-FeGS provided sufficient adsorption sites for the adsorption of Mn²⁺. For Fe 2p spectra (Fig. 4e), the two strong peaks located at 711.3 and 725.1 eV were assigned to Fe 2p_{3/2} and Fe

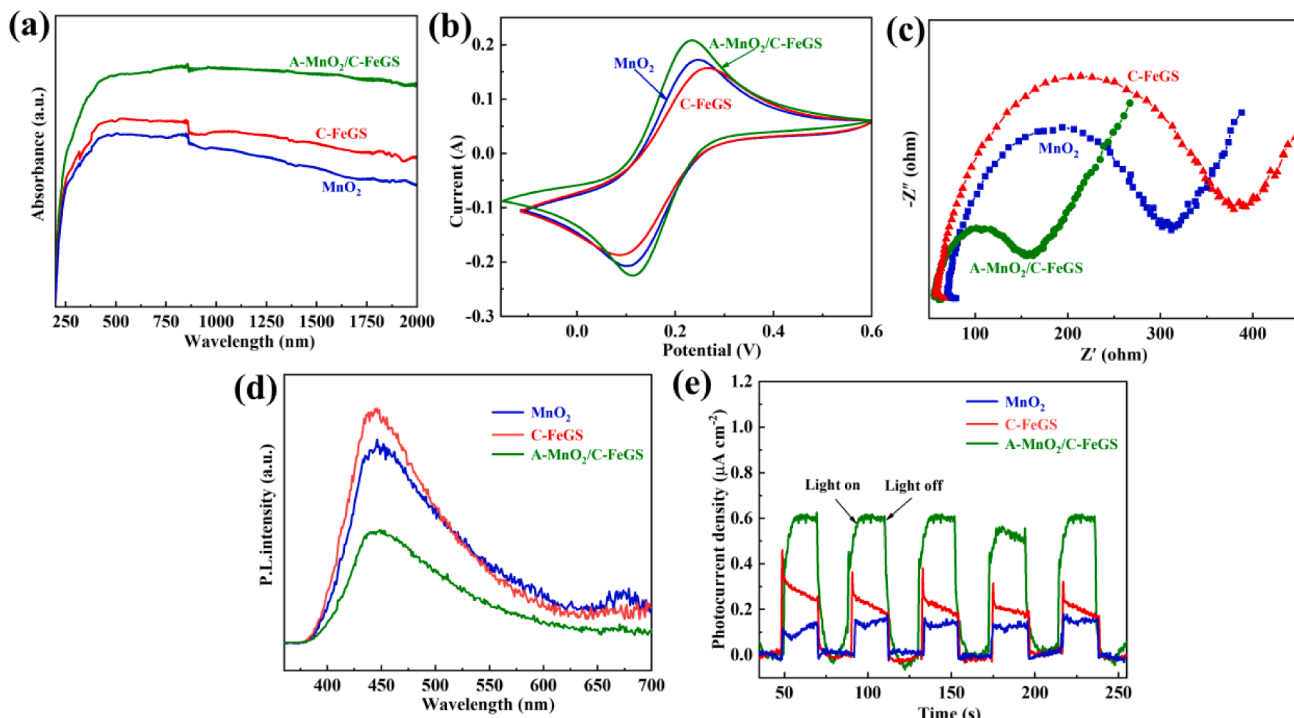


Fig. 5. (a) UV-Vis-NIR adsorption spectra, (b) CV curves, (c) EIS data, (d) PL spectra, and (e) transient photocurrent responses of MnO_2 , C-FeGS, and A- $\text{MnO}_2/\text{C-FeGS}$.

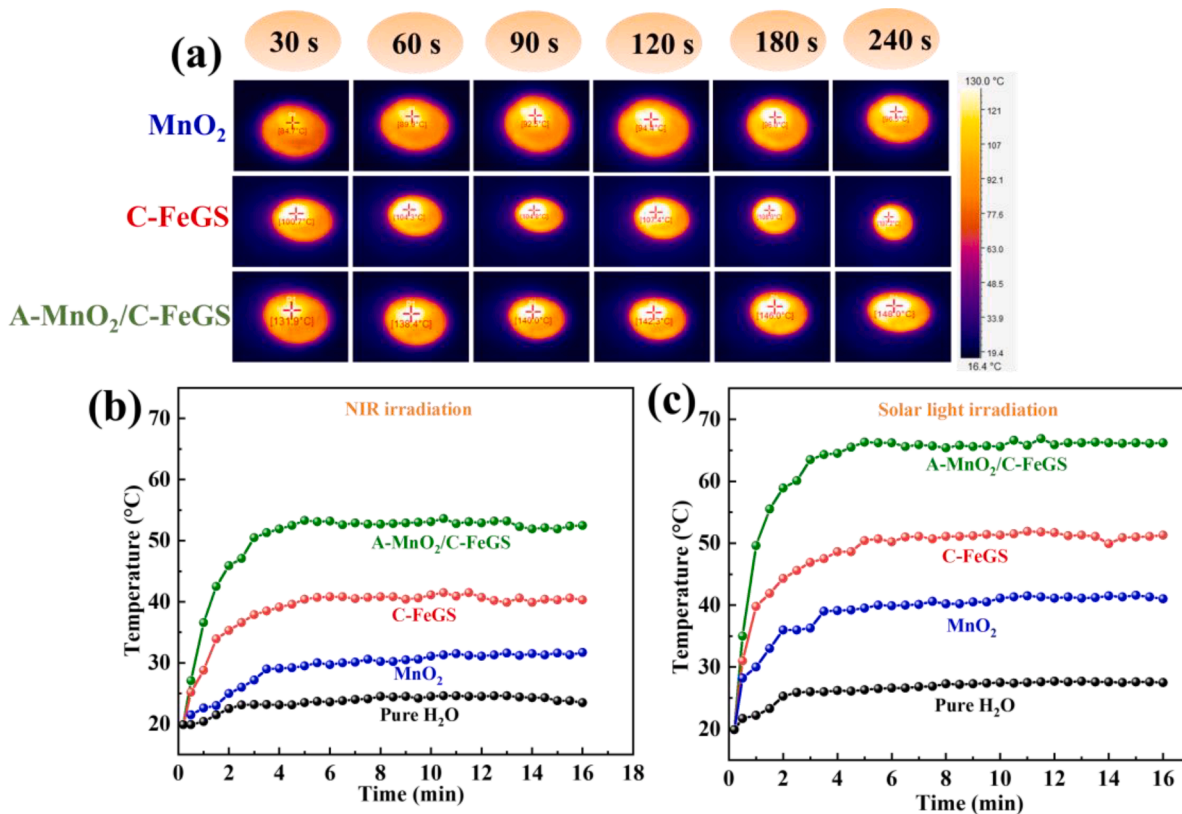


Fig. 6. (a) Thermal images of MnO_2 , C-FeGS, and A- $\text{MnO}_2/\text{C-FeGS}$ under Xenon lamp irradiation; temperature versus time plots recorded in water and the MnO_2 , C-FeGS, and A- $\text{MnO}_2/\text{C-FeGS}$ reaction systems under (b) NIR irradiation and (c) Xenon lamp irradiation.

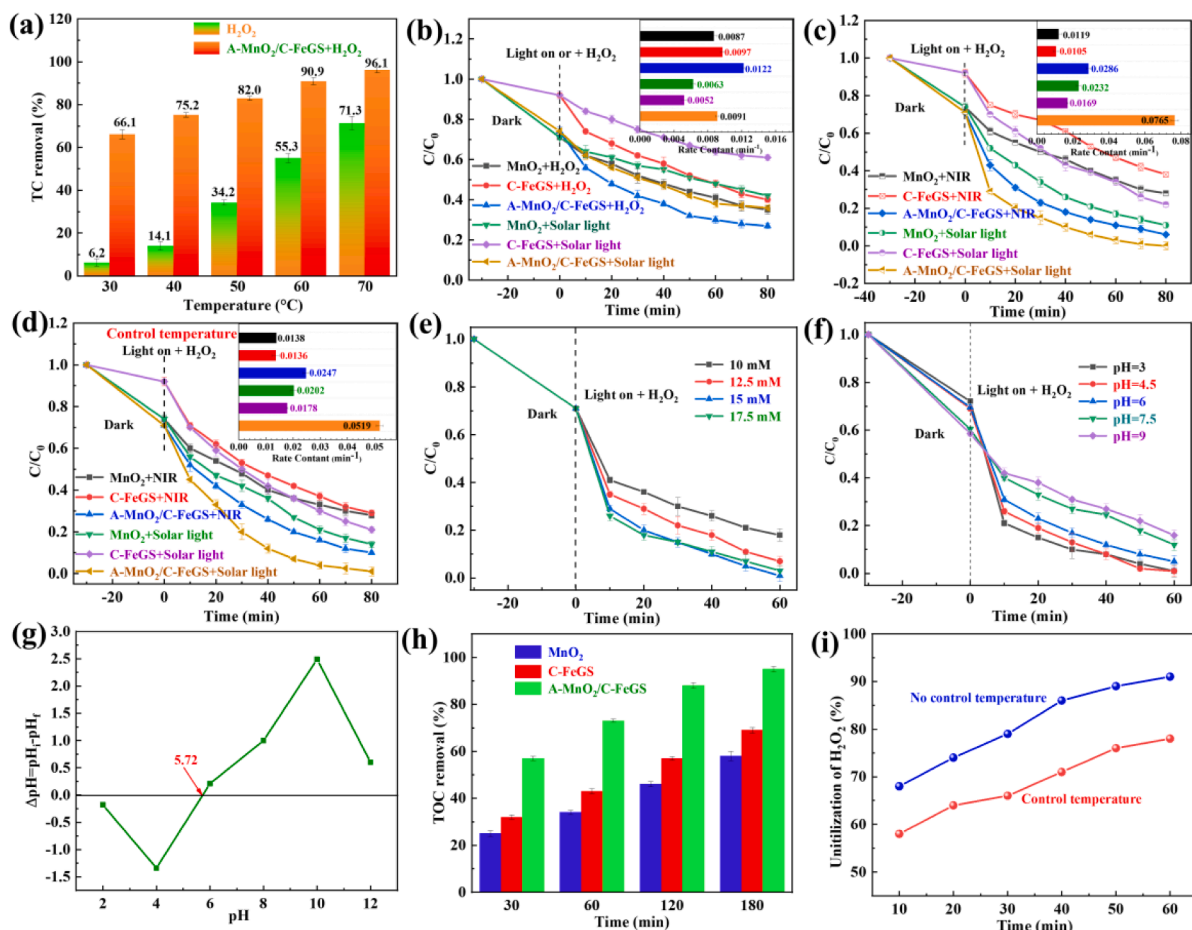


Fig. 7. (a) TC removal in H_2O_2 and A-MnO₂/C-FeGS+ H_2O_2 systems at different temperatures; TC removal in different reaction systems: (b) photo and Fenton-like systems and the corresponding kinetic constants, (c) photo-Fenton system under solar light and NIR irradiation and the corresponding kinetic constants, and (d) photo-Fenton reaction under solar light and NIR irradiation with temperature control at 25 °C and the corresponding kinetic constants; effects of (e) H_2O_2 concentration and (f) initial pH value on TC removal over A-MnO₂/C-FeGS; (g) Zeta potential of A-MnO₂/C-FeGS; (h) TOC removal and (i) H_2O_2 utilization rate in A-MnO₂/C-FeGS+ H_2O_2 system under solar light irradiation. Reaction conditions: $\text{H}_2\text{O}_2 = 15 \text{ mM}$, initial pH = 5.5, TC = 50 mg L⁻¹, and catalyst dosage = 2 g L⁻¹.

$2p_{1/2}$ [7], respectively. The slight shift of the peaks in Fe 2p spectrum after in-situ growth of MnO₂ was ascribed to the chemical interaction between Fe₃O₄ and A-MnO₂. As shown in Fig. 4f, the Mn $2p_{3/2}$ (642.5 eV) could be fitted to three peaks located at 640.8, 642.3, and 643.6 eV, denoted as Mn²⁺, Mn³⁺, and Mn⁴⁺, respectively [20]. The surface content of Mn²⁺+Mn³⁺ in A-MnO₂/C-FeGS (82.5%) was much higher than that in MnO₂ (60.1%). Generally, the increased content of lower valent Mn means the formation of more crystal defects and oxygen vacancies, which is favorable for photocatalysis by trapping more electrons and provides more active sites for activating reactive species [43]. Therefore, the increased content of oxygen vacancy and the reduction in Mn valence indicate the abundant structural defects in A-MnO₂/C-FeGS.

3.2. Photochemical properties of the catalysts

The optical properties of MnO₂, C-FeGS, and A-MnO₂/C-FeGS were characterized by UV-vis-NIR DRS spectra. Fig. 5a shows that these three catalysts had light absorption ability in the full light spectrum, including UV, Vis, and NIR regions. MnO₂ showed relatively lower light adsorption capacity especially in the NIR region, which could be ascribed to its intrinsic bandgap transition. While C-FeGS showed relatively higher light adsorption capacity than MnO₂, attributed to the strong light absorption ability of C. After in-situ growth of A-MnO₂, the absorbance of A-MnO₂/C-FeGS was greatly enhanced, making it possible to full use the solar light. This can be attributed to that the doped Na⁺ induced the

change and reduction in the bandgap of MnO₂ [45], and the absorbed light could be refracted and reflected repeatedly between nano-tentacles and porous channels, thus greatly enhancing the light absorption performance.

To understand the charge transfer properties of the as-prepared catalysts, several electrochemical measurements were performed. It is known that higher photocurrent corresponds to an increase in photo-generated electrons transfer rate. Fig. 5b presents that the photocurrent response of A-MnO₂/C-FeGS was obviously higher than that of C-FeGS and MnO₂, confirming the increased photo-induced charge separation and transfer capacity of A-MnO₂/C-FeGS. The charge separation and migration properties of the catalysts were determined by EIS test. In general, smaller arc radius corresponds to smaller impedance resistance and higher charge transfer ability. As shown in Fig. 5c, the smaller arc radius of MnO₂ revealed the relatively higher photogenerated e⁻-h⁺ ability. Furthermore, the resistance of A-MnO₂/C-FeGS was smallest among the three catalysts, indicating that A-MnO₂/C-FeGS possessed excellent separation and transformation efficiency of photo-generated e⁻-h⁺. Furthermore, PL spectra of the samples were used to investigate the recombination of photogenerated charges. Generally, lower PL intensity means lower recombination rate of e⁻-h⁺. C-FeGS showed the highest fluorescence peak at 400–650 nm (Fig. 5d), indicating its highest recombination rate of photo-generated e⁻-h⁺. While the fluorescence intensity of A-MnO₂/C-FeGS was significantly decreased compared with C-FeGS, demonstrating the lower recombination rate of e⁻-h⁺. The

transient photocurrent density can directly reflect the separation efficiency of photogenerated e^-h^+ and the migration rate of charges [46]. As depicted in Fig. 5e, A-MnO₂/C-FeGS showed the highest photocurrent density, suggesting the fast charge transfer occurred in A-MnO₂/C-FeGS. The higher separation efficiency of photogenerated e^-h^+ and the migration rate of charges in A-MnO₂/C-FeGS, owing to that the abundant defects in amorphous MnO₂ could capture electrons, which were secondly transited to conduction band under thermal activation. Meanwhile, the excellent electron transport capacity of C could effectively reduce the recombination rate of photo-generated e^-h^+ , leading to better photocatalytic performance.

3.3. IR thermal images analysis

To explore the full light-driven thermo-catalysis, the surface temperature of the catalysts and the solution temperature of different reaction systems were monitored by an IR thermal camera after exposure to Xenon lamp for 10 min. Fig. 6a shows that the surface temperature of MnO₂ quickly reached 84.7 °C after irradiation for 30 s, and further increased to 96.5 °C after 4 min. This is due to the thermal effect of e^-h^+ generated by the d-d transition of Mn ions in MnO₂ [43,47]. As for C-FeGS, the surface temperature quickly increased to 100.7 °C within 30 s, and further increased to 108.1 °C with the increase of irradiation time, which could be attributed to the strong light absorption ability of the decorated C. After in-situ growth of A-MnO₂, the surface temperature of A-MnO₂/C-FeGS significantly reached to 131.9 °C within only 30 s, which could be attributed to the synergy of flower ball shaped amorphous MnO₂ and C decoration. The disordered structure and rich oxygen vacancies could greatly enhance the photo-thermal synergistic effect of the catalyst, and thus increased its photo-thermal conversion performance. The rapid increase in surface temperature of the catalyst could greatly increase the adsorption of MnO₂ to O₂ and accelerate the secondary transition and utilization of thermal electrons captured by the defect sites, thus generating more $\cdot O_2^-$ for oxidative degradation of TC. In addition, the solution temperature was monitored to directly investigate the photo-thermal conversion ability. As shown in Fig. 6b and c, a significant increase in the solution temperature of A-MnO₂/C-FeGS reaction system was observed both irradiated with NIR and full light, with the temperature of 66.3 °C under full light irradiation and 53.6 °C under NIR irradiation after 4 min, which was obviously higher than MnO₂ reaction system (41.3 °C under full light irradiation and 31.7 °C under NIR irradiation) and C-FeGS reaction system (51.8 °C under full light irradiation and 41.5 °C under NIR irradiation). This further demonstrates the strong photo-thermal conversion ability of A-MnO₂/C-FeGS. The enhanced photo-thermal effect could be attributed to the excellent full spectrum response and the repeated refraction and reflection between nano-tentacles and porous channels resulted from the combination of amorphous MnO₂ and C, and thus greatly accelerated the in-situ heat of the catalyst and the activation of H₂O₂.

3.4. Photocatalytic performance of the catalysts

The above characterizations clearly demonstrate that the light adsorption ability and the transfer and separation efficiency of photogenerated e^-h^+ were significantly enhanced after in-situ growth A-MnO₂ on C-FeGS, which is favorable for the improvement of photocatalytic performance. The photo-thermal-Fenton catalytic performances of MnO₂, C-FeGS and A-MnO₂/C-FeGS were comparatively estimated with TC as the target organic contaminant. Firstly, the degradation of TC by H₂O₂ activated at different temperatures were performed. As shown in Fig. 7a, the solution temperature exhibited great influence on TC removal. When the temperature was above 70 °C, 71.3% TC removal rate could be obtained. Notably, the TC removal rate was significantly increased from 66.1% to 96.1% with the temperature increasing from 30 to 70 °C over the A-MnO₂/C-FeGS catalyst within 80 min. This phenomenon obviously demonstrates that the temperature

had a great influence on the activation of H₂O₂. As shown in Fig. 7b, A-MnO₂/C-FeGS exhibited higher adsorption performance with TC removal rate of 26.3% within 30 min compared with C-FeGS (8.1%), attributed to the higher BET surface area induced by the in-situ growth of amorphous MnO₂. The MnO₂ showed relatively superior catalytic performance both in Fenton and photocatalytic systems than C-FeGS, which could be attributed to the intrinsic photocatalytic performance and the activation of H₂O₂ by variable valence of Mn. After in-situ growth of amorphous MnO₂, the A-MnO₂/C-FeGS displayed excellent catalytic performance both in Fenton and photocatalytic systems. The degradation performance was also confirmed by the degradation constant rate. A-MnO₂/C-FeGS possessed the highest constant rate (0.0091 min⁻¹ in Fenton system and 0.0122 min⁻¹ in photocatalytic system) compared with MnO₂ (0.0063 min⁻¹ in Fenton system and 0.0087 min⁻¹ in photocatalytic system) and C-FeGS (0.0052 min⁻¹ in Fenton system and 0.0097 min⁻¹ in photocatalytic system). This can be ascribed to the strong interaction of Fe-Mn and higher photo-thermal conversion efficiency of the catalyst, which could greatly accelerate the charge transfer and utilization rate, thus producing more radicals. Moreover, the amorphous MnO₂ with rich oxygen vacancies in octahedron could provide more active sites.

To further verify the utilization efficiency of light, solar light and NIR light were applied for comparative investigation (Fig. 7c). Notably, A-MnO₂/C-FeGS displayed the highest degradation efficiency and constant rate both in solar light irradiation and NIR light irradiation systems, with almost 4.5 and 3.3 times higher than MnO₂ and C-FeGS under solar light irradiation. This can be ascribed to that the synergy of the carbon layer and the A-MnO₂ with flower structure could induce multiple reflection of the adsorbed light inner A-MnO₂/C-FeGS to make full use of solar energy and obtain excellent photo-thermal conversion. In addition, to clearly understand the influence of solution temperature on the reaction efficiency, the photo-thermal-Fenton reaction was performed at 25 °C in a constant temperature water bath. As shown in Fig. 7d, the TC removal rate was significantly decreased both under solar light and NIR irradiation with controlling reaction temperature at 25 °C, indicating that the solution temperature was important to the activation of H₂O₂. However, nearly 100% of TC removal rate within 60 min was obtained in A-MnO₂/C-FeGS+H₂O₂+solar light system at 25 °C, attributed to that the higher surface temperature of the catalyst could in-situ activate the electrons in the defect sites and accelerate the electron transition to produce more free radicals.

The effect of H₂O₂ concentration was investigated (Fig. 7e), and the result indicates that the relatively lower TC removal rate obtained in both lower and higher H₂O₂ concentration, ascribed to the lower generation rate of $\cdot OH$ in lower H₂O₂ concentration and the trapping of $\cdot OH$ in higher H₂O₂ concentration [48]. Thus, the suitable H₂O₂ concentration was 15 mmol L⁻¹. Subsequently, the effect of initial pH value on TC degradation catalyzed by A-MnO₂/C-FeGS was investigated. As shown in Fig. 7f, the pH value showed remarkable effect on the adsorption and degradation of TC. Generally, the surface charge of the catalyst is associated with its adsorption performance, thus affecting its degradation performance. The PZC value of A-MnO₂/C-FeGS was estimated to be 5.72 (Fig. 7g), indicating that the surface charge was positive at pH < 5.72 and negative at pH > 5.72. While the TC exists in the form of positively charged molecule at acid conditions (pH < 7.68) and non-charged or negatively charged at basic conditions [48]. Therefore, the A-MnO₂/C-FeGS catalyst showed excellent adsorption performance at relatively basic conditions. The degradation efficiency of TC was sharply decreased when pH value increased to 9.5, ascribed to that the reaction between OH⁻ and metal ions suppressed the interaction between Fe/Mn species with H₂O₂, resulting in the production of less $\cdot OH$. At a lower pH value, the abundant H⁺ was conducive to the cycle of Fe³⁺/Fe²⁺ and Mn⁴⁺/(Mn²⁺+Mn³⁺), leading to higher degradation rate. However, the dissolution of metal ions in relatively lower pH value may affect the reusability of the catalyst. Thus, an optimum pH of 5.5 was adopted in the following exploration.

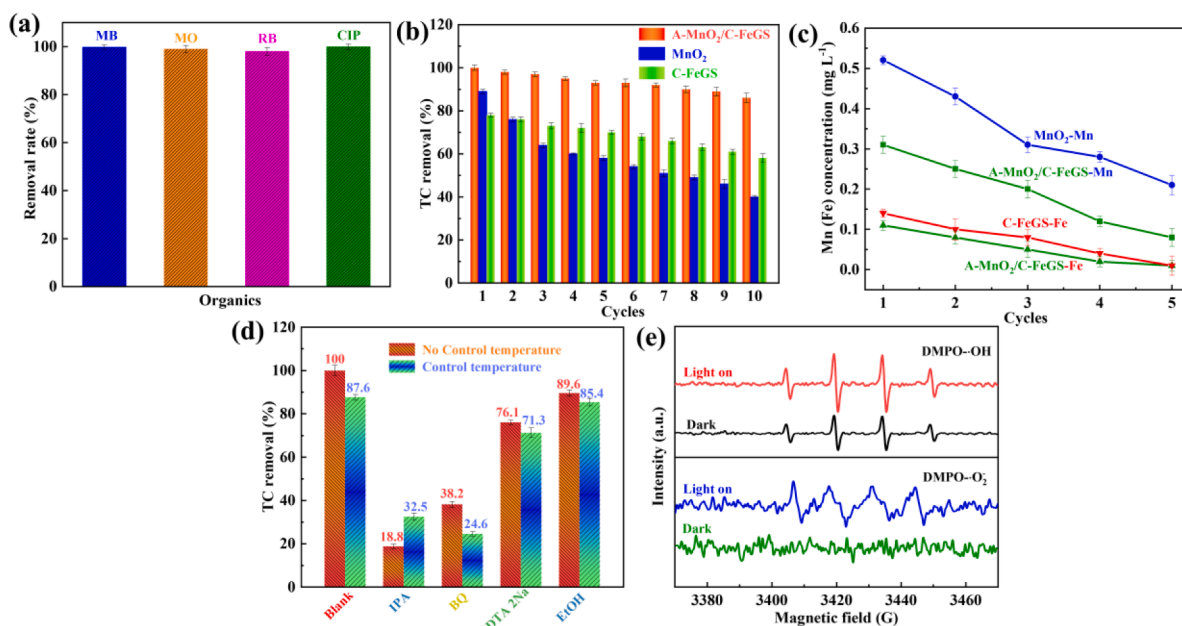


Fig. 8. (a) Removal rates of various organics in A-MnO₂/C-FeGS+H₂O₂+solar light system; (b) recyclability and (c) corresponding concentrations of leached Fe and Mn in the degradation process of TC over MnO₂, C-FeGS, and A-MnO₂/C-FeGS; (d) quenching experiment and (e) ESR spectra of DMPO-O₂ and DMPO-OH in A-MnO₂/C-FeGS+H₂O₂ system.

Furthermore, the mineralization degree of TC over different photocatalyst was estimated by TOC analysis. As shown in Fig. 7h, the TOC removal of TC catalyzed by A-MnO₂/C-FeGS was 95.5% within 180 min, while only 58.3% and 69.2% of TOC removal were obtained over MnO₂ and C-FeGS catalysts, respectively. The higher TOC removal rate further demonstrates the excellent catalytic performance of A-MnO₂/C-FeGS in photo-thermal-Fenton reaction. In addition, the utilization rates of H₂O₂

in two systems were analyzed to explore the in-situ photo-thermal effect and the activation of H₂O₂ by heat in solution during the degradation process (Fig. 7i). With the increase of reaction time, the utilization rate of H₂O₂ in the system without temperature control could be greatly increased to 91.3%, which was much higher than in the system with temperature control at 25 °C (78.5%). This indicates the strong enhancement of photo-induced in-situ heating and heat-induced

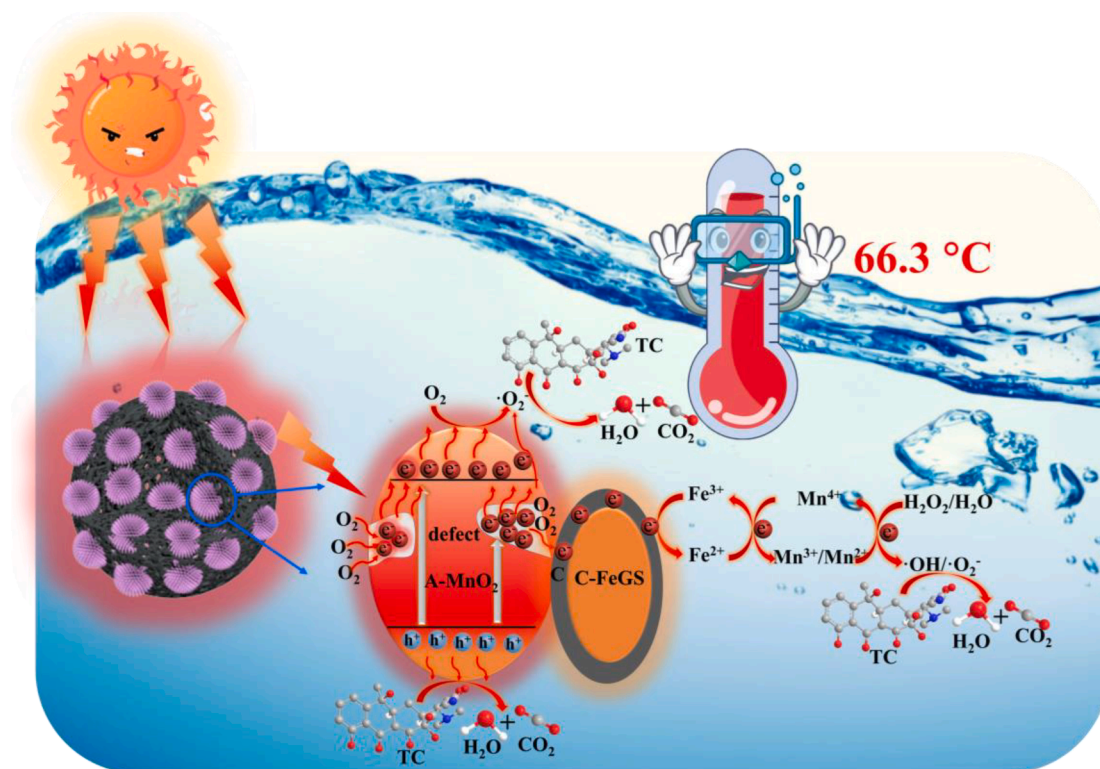


Fig. 9. Schematic illustration of photo-thermal-Fenton catalytic mechanism over A-MnO₂/C-FeGS under solar light irradiation.

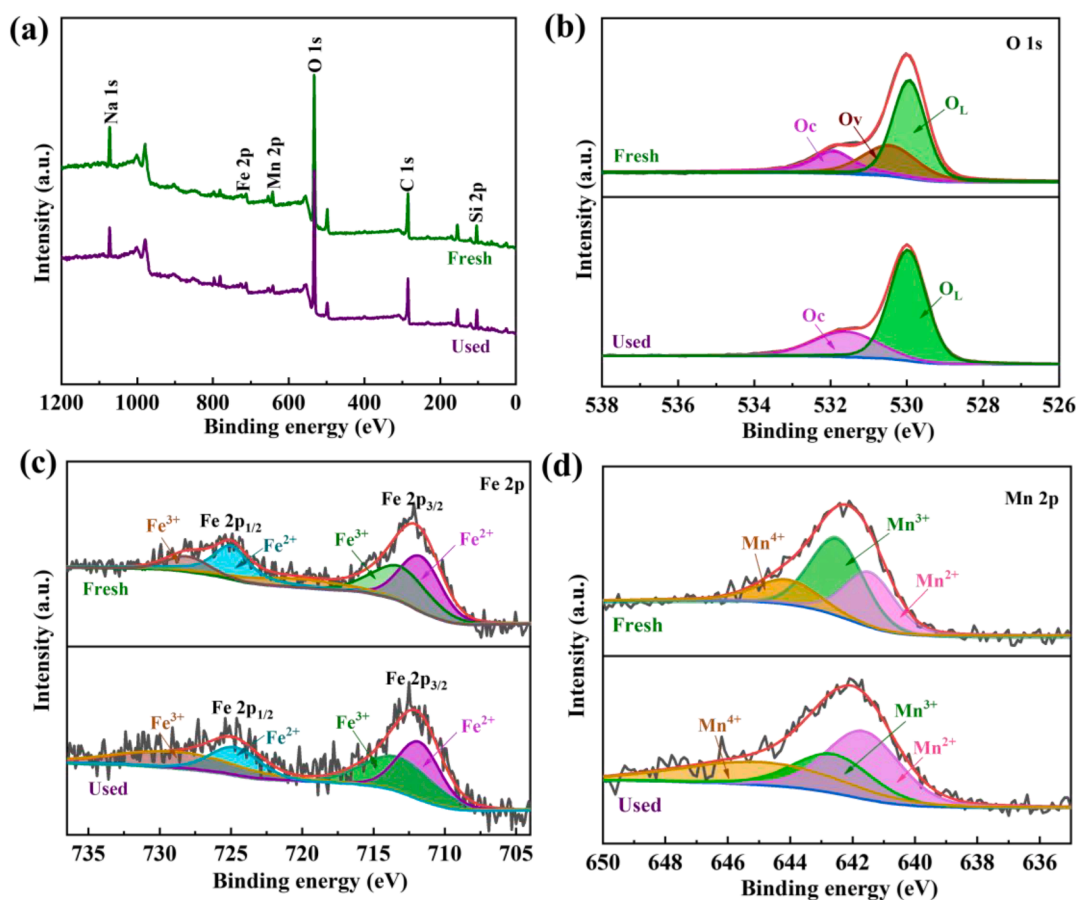


Fig. 10. XPS spectra of the A-MnO₂/C-FeGS catalyst before and after reaction: (a) full survey scan, (b) peak fitting curves of O 1s spectra, (c) Fe 2p spectra, and (d) Mn 2p spectra.

activation of H₂O₂ in photo-Fenton reaction.

3.5. Cycle stability and reusability of the catalysts

To investigate the adaptability of the A-MnO₂/C-FeGS catalyst, the catalytic performance toward various organic pollutants with different structures was carried out. As shown in Fig. 8a, the A-MnO₂/C-FeGS+H₂O₂+solar light system exhibited excellent degradation performance with the removal rates all > 98% for MB, MO, RB, and CIP, demonstrating the outstanding adaptability of A-MnO₂/C-FeGS for treating different organic pollutants. The recyclability of MnO₂, C-FeGS, and A-MnO₂/C-FeGS was explored by ten consecutive recycling degradation tests. A-MnO₂/C-FeGS showed the highest stability with the TC removal rates all > 88% in ten degradation cycles (Fig. 8b). Notably, the TC removal rate was low (40% in the tenth cycle) when catalyzed by MnO₂, which may be ascribed to the leaching of Mn ions in the solution. C-FeGS showed relatively higher stability compared with MnO₂, with TC removal rate decreased from 78% to 60% after ten cycles. The geopolymer and decorated-C are responsible for the stabilization of metal ions, ascribed to the formation of an intimate interfacial structure between C and Fe₃O₄ in reduction roasting process. The enriched electrons on the surface of C can effectively protect the metal ions from being oxidized and leached in photocatalytic process. The concentrations of leached Mn and Fe ions in the five cycles were further estimated by FAAS analysis (Fig. 8c). In the first cycle, 0.53 mg L⁻¹ of Mn ions was detected in the MnO₂ reaction system, which was much higher than that in the A-MnO₂/C-FeGS reaction system (0.12 mg L⁻¹), and all decreased after each cycle. While lower concentrations of Fe ions were detected both in the C-FeGS and A-MnO₂/C-FeGS reaction systems, further

demonstrating the stabilizing effect of C-FeGS for A-MnO₂. In addition, the XRD patterns and FTIR spectra of A-MnO₂/C-FeGS showed a negligible change in the phase and morphology after reaction (Fig. S2a–b), indicating the excellent stability of the A-MnO₂/C-FeGS catalyst.

3.6. Possible photocatalytic mechanism

To clarify the predominant radical species in the photo-thermal-Fenton process, ESR tests and capture experiments were exerted over A-MnO₂/C-FeGS. As shown in Fig. 8e, strong four signals of DMPO-·OH were observed both in dark and light irradiation system, confirming the generation of ·OH in the system [49]. While the intensity of ·OH became stronger when light on, demonstrating that more reactive species were generated under light irradiation. In addition, four signals with intensity ratio of 1:1:1:1 corresponding to DMPO-·O₂ were observed under light irradiation. Whereas, the featured signals of DMPO-·O₂ were undetectable in dark, suggesting that the generation of ·O₂ radicals only occurred in the light irradiation process. To further determine the main active species for degrading TC catalyzed by A-MnO₂/C-FeGS, the quenching experiments were performed. Fig. 8d shows that the TC removal rate was significantly decreased with the addition of IPA and BQ, suggesting that ·OH and ·O₂ played a crucial role in TC degradation. While the TC removal rate decreased to 76.1% and 89.6% in the presence of EDTA-2Na and EtOH scavengers, respectively. The free radicals scavenging experiments presented that ·OH and ·O₂ were responsible for the degradation of TC and h⁺ and e⁻ also participated in the degradation process. In the photo-Fenton reaction system with temperature control at 25 °C, all the removal rates of TC were visibly decreased, and the radicals contribution changed from ·OH > ·O₂ > h⁺ > e⁻ to ·O₂ > ·OH >

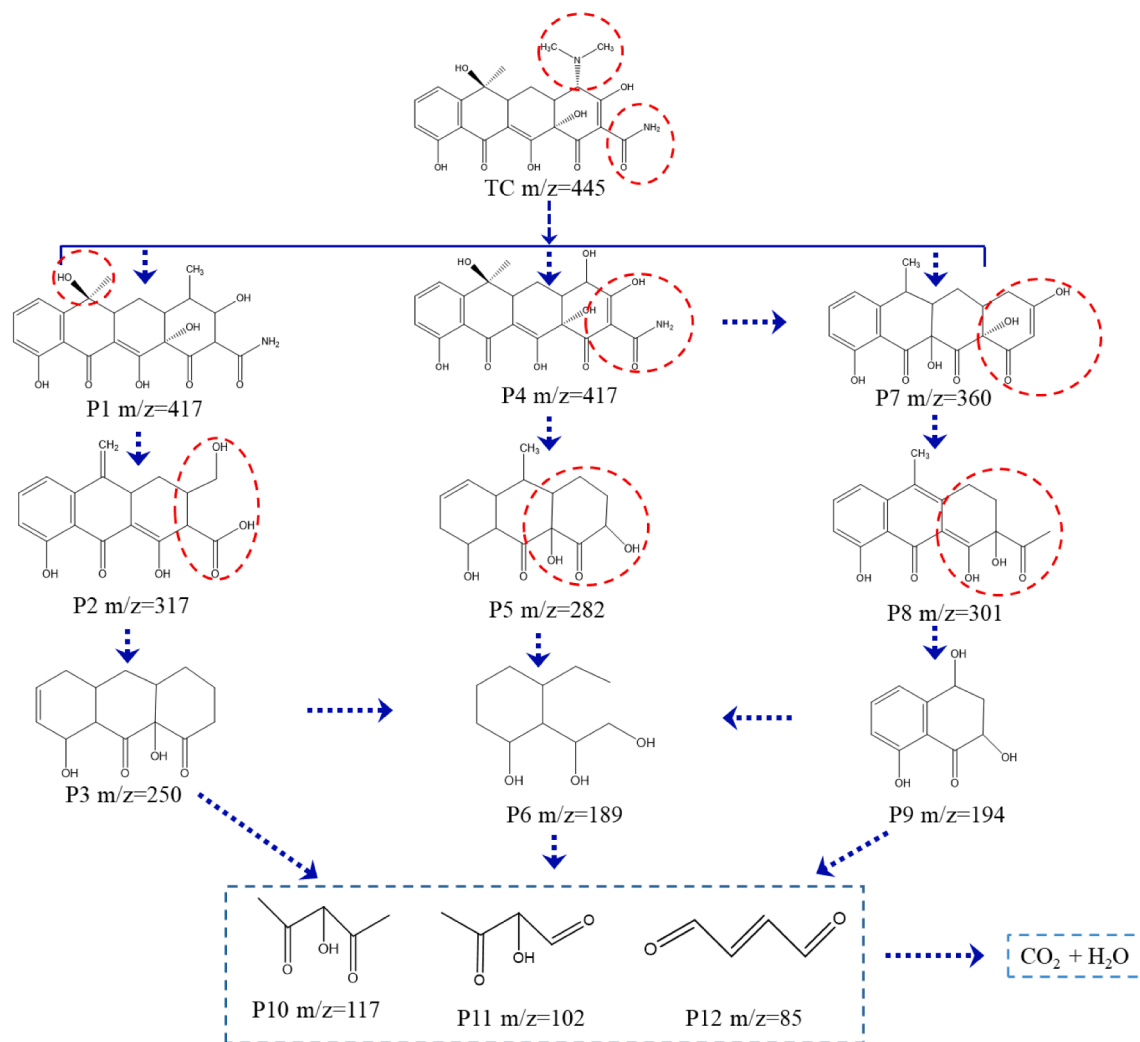
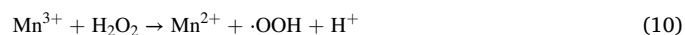
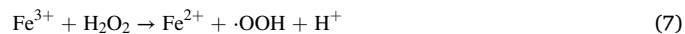


Fig. 11. Possible catalytic degradation pathways of TC in photo-thermal-Fenton process over A-MnO₂/C-FeGS.

$h^+ > e^-$. This could be attributed to that the rapidly increased surface temperature of the catalyst induced by photo-thermal greatly increased the adsorption of amorphous MnO₂ to surface O₂ and accelerated the secondary transition and utilization of thermal electrons captured by the defect sites, thus generating more $\cdot O_2^-$ for oxidative degradation of TC.

XPS analysis was performed to further estimate the surface characteristics of A-MnO₂/C-FeGS before and after reaction. As presented in Fig. 10a, no significant changes were observed in the full XPS spectrum after reaction, demonstrating the excellent stability of A-MnO₂/C-FeGS. O 1s XPS spectrum (Fig. 10b) showed a great change after reaction as the total consumption of oxygen vacancy, indicating that oxygen vacancy was involved in the whole degradation process. After reaction, the percentages of Fe²⁺ and Fe³⁺ were changes from 59.2% and 40.8% to 46.9% and 53.1%, respectively. As for Mn 2p, the content of Mn²⁺+Mn³⁺ and Mn⁴⁺ changed from 82.5% and 17.5% to 62.6% and 31.4%, respectively. These changes in the valence states of surface Mn, O, and Fe indicate the good circle of Fe³⁺/Fe²⁺ and Mn⁴⁺/(Mn²⁺+Mn³⁺), which is favorable for the production of $\cdot OH$. Based on above results and analysis, a proposed catalytic mechanism in A-MnO₂/C-FeGS+H₂O₂+solar light system is shown in Fig. 9, and the possible involved reaction steps are summarized as following:



3.7. TC degradation pathways

HPLC-MS technique was employed to detect the transformation products of TC in the degradation process. As presented in Fig. S3,

twelve kinds of intermediate compounds were monitored in the process, with m/z (mass to charge ratio) values of 417 (P1), 359 (P2), 250 (P3), 417 (P4), 281 (P5), 189 (P6), 360 (P7), 301 (P8), 194 (P9), 117 (P10), 102 (P11), and 85 (P12). The possible degradation pathways were proposed and shown in Fig. 11. There are three possible degradation pathways. Firstly, TC was deaminated and dehydrated to form P1, P4, and P7. Then, the destruction of the C=C on the benzene ring, decarboxylation, and dehydroxylation led to the formation of the intermediate products, including P2, P3, P5, P8, and P9. Subsequently, the benzene ring was attacked by free radicals and oxidized to form the compounds of P6 and P11–P13. Finally, these products could be further oxidized and completely decomposed to CO_2 and H_2O with sufficient reaction time [49–52].

4. Conclusion

In summary, a novel A-MnO₂/C-FeGS catalyst with rich oxygen vacancies was successfully fabricated by a persulfate oxidation method in Na⁺-containing solution, and was applied as an efficient catalyst for the degradation of TC in solar light-induced photo-thermal-Fenton process. A-MnO₂/C-FeGS exhibited excellent catalytic performance for TC degradation, with TC removal of 98.2% within 30 min and TOC removal of 95.5% within 180 min, which were much higher than MnO₂ and C-FeGS. The excellent activity of A-MnO₂/C-FeGS was attributed to that the photo-thermal conversion in-situ heated the catalyst and induced the activation of H₂O₂, and the abundant structural defects could provide more catalytic active sites and full spectrum light absorption capacity. Furthermore, the thermal energy could be rapidly transferred to MnO₂ through C, promoting the activation of the surface lattice oxygen and accelerating the secondary transition and utilization of the thermal electrons captured by the defect sites. This resulted in efficient separation of e⁻-h⁺ and utilization rate of thermal electrons, which could effectively accelerate electron transfer and the redox cycles of Fe³⁺/Fe²⁺ and Mn⁴⁺/(Mn²⁺+Mn³⁺), thus enhancing the catalytic activity of A-MnO₂/C-FeGS. The free radical contribution was ·OH > ·O₂⁻ > h⁺ > e⁻ in photo-thermal-Fenton process, and changed to ·O₂⁻ > ·OH > h⁺ > e⁻ with temperature control at 25 °C, further confirming the photo-thermal activation of H₂O₂. In addition, A-MnO₂/C-FeGS maintained high performance after ten cycles, ascribed to the favorable structural stability. Therefore, the systematic studies indicate that in-situ growth of A-MnO₂ on C-FeGS can greatly boost the catalytic performance, and provide a feasible insight for the construction of MnO₂-based functional materials with unique structure and excellent catalytic activity for environmental remediation.

Declaration of Competing Interest

The authors declare that they have no known competing financial interests or personal relationships that could have appeared to influence the work reported in this paper.

Data availability

Data will be made available on request.

Acknowledgements

This research was supported by National Natural Science Foundation of China (Nos. 22068007 and 22008041), Natural Science Foundation of Guangxi Province, China (Nos. 2019GXNSFDA245020 and 2020GXNSFGA297001), and the Innovation Project of Guangxi Graduate Education (No. YCBZ2021023).

Appendix A. Supplementary data

Supplementary data to this article can be found online at <https://doi.org/10.1016/j.cej.2022.137857>.

[org/10.1016/j.cej.2022.137857](https://doi.org/10.1016/j.cej.2022.137857).

References

- [1] Y. Zhang, Z. Wang, X. Yang, Y. Zhu, H. Wang, Afterglow-catalysis and molecular imprinting: A promising union for elevating selectivity in degradation of antibiotics, *Appl. Catal. B-Environ.* 305 (2022), 121025.
- [2] F. Guo, H. Zhang, H. Li, Z. Shen, Modulating the oxidative active species by regulating the valence of palladium cocatalyst in photocatalytic degradation of ciprofloxacin, *Appl. Catal. B-Environ.* 306 (2022), 121092.
- [3] L. Jing, Y. Xu, J. Liu, M. Zhou, H. Xu, M. Xie, H. Li, J. Xie, Direct Z-scheme red carbon nitride/rod-like lanthanum vanadate composites with enhanced photodegradation of antibiotic contaminants, *Appl. Catal. B-Environ.* 277 (2020), 119245.
- [4] H. Wang, T. Chen, D. Chen, X. Zou, M. Li, F. Huang, F. Sun, C. Wang, D. Shu, H. Liu, Sulfurized oolitic hematite as a heterogeneous Fenton-like catalyst for tetracycline antibiotic degradation, *Appl. Catal. B-Environ.* 260 (2020), 118203.
- [5] X. Zhang, B. Xu, S. Wang, X. Li, C. Wang, Y. Xu, R. Zhou, Y. Yu, H. Zheng, P. Yu, Y. Sun, Carbon nitride nanotubes anchored with high-density Cu_{Nx} sites for efficient degradation of antibiotic contaminants under photo-Fenton process: Performance and mechanism, *Appl. Catal. B-Environ.* 306 (2022), 121119.
- [6] Z. Zhong, M. Li, J. Fu, Y. Wang, Y. Muhammad, S. Li, J. Wang, Z. Zhao, Z. Zhao, Construction of Cu-bridged Cu₂O/MIL(Fe/Cu) catalyst with enhanced interfacial contact for the synergistic photo-Fenton degradation of thiacloprid, *Chem. Eng. J.* 395 (2020), 125184.
- [7] J. Jiang, X. Wang, Y. Liu, Y. Ma, T. Li, Y. Lin, T. Xie, S. Dong, Photo-Fenton degradation of emerging pollutants over Fe-POM nanoparticle/porous and ultrathin g-C₃N₄ nanosheet with rich nitrogen defect: Degradation mechanism, pathways, and products toxicity assessment, *Appl. Catal. B-Environ.* 278 (2020), 119349.
- [8] X. Liu, J. Zhou, D. Liu, L. Li, W. Liu, S. Liu, C. Feng, Construction of Z-scheme CuFe₂O₄/MnO₂ photocatalyst and activating peroxymonosulfate for phenol degradation: Synergistic effect, degradation pathways, and mechanism, *Environ Res* 200 (2021), 111736.
- [9] J. Wang, T. Xie, G. Han, Q. Zhu, Y. Wang, Y. Peng, S. Liu, Z. Yao, SiO₂ mediated templating synthesis of γ-Fe₂O₃/MnO₂ as peroxymonosulfate activator for enhanced phenol degradation dominated by singlet oxygen, *Appl. Surf. Sci.* 560 (2021), 149984.
- [10] Y. Ding, C. Pan, X. Peng, Q. Mao, Y. Xiao, L. Fu, J. Huang, Deep mineralization of bisphenol A by catalytic peroxymonosulfate activation with nano CuO/Fe₃O₄ with strong Cu-Fe interaction, *Chem. Eng. J.* 384 (2020), 123378.
- [11] R. Wang, Q. Hao, J. Feng, G. Wang, H. Ding, D. Chen, B. Ni, Enhanced separation of photogenerated charge carriers and catalytic properties of ZnO-MnO₂ composites by microwave and photothermal effect, *J. Alloy. Compd.* 786 (2019) 418–427.
- [12] P. Dong, X. Chen, M. Guo, Z. Wu, H. Wang, F. Lin, J. Zhang, S. Wang, C. Zhao, H. Sun, Heterogeneous electro-Fenton catalysis with self-supporting CFP/MnO₂-Fe₃O₄/C cathode for shale gas fracturing flowback wastewater, *J. Hazard. Mater.* 412 (2021), 125208.
- [13] M. Zhang, B. Li, Y. Du, G. Zhou, Y. Tang, Y. Shi, B. Zhang, Z. Xu, Q. Huang, A novel intelligent PANI/PPy@Au/MnO₂ yolk-shell nanozyme for MRI-guided 'triple-mode' synergistic targeted anti-tumor therapy, *Chem. Eng. J.* 424 (2021), 130356.
- [14] B. Ma, Y. Nishina, A. Bianco, A glutathione responsive nanoplatform made of reduced graphene oxide and MnO₂ nanoparticles for photothermal and chemodynamic combined therapy, *Carbon* 178 (2021) 783–791.
- [15] Y. Cai, R. Chua, S. Huang, H. Ren, M. Srinivasan, Amorphous manganese dioxide with the enhanced pseudocapacitive performance for aqueous rechargeable zinc-ion battery, *Chem. Eng. J.* 396 (2020), 125221.
- [16] S. Devaraj, N. Munichandraiah, Effect of Crystallographic Structure of MnO₂ on Its Electrochemical Capacitance Properties, *J. Phys. Chem. C* 112 (2008) 4406–4417.
- [17] W. Zeng, H. Zhang, Y. Deng, A. Jiang, X. Bao, M. Guo, Z. Li, M. Wu, X. Ji, X. Zeng, L. Mei, Dual-response oxygen-generating MnO₂ nanoparticles with polydopamine modification for combined photothermal-photodynamic therapy, *Chem. Eng. J.* 389 (2020), 124494.
- [18] J. Ye, M. Zhou, Y. Le, B. Cheng, J. Yu, Three-dimensional carbon foam supported MnO₂/Pt for rapid capture and catalytic oxidation of formaldehyde at room temperature, *Appl. Catal. B-Environ.* 267 (2020), 118689.
- [19] Y. Xiang, N. Li, L. Guo, H. Wang, H. Sun, R. Li, L. Ma, Y. Qi, J. Zhan, D. Yu, Biocompatible and pH-sensitive MnO₂-loaded carbonaceous nanospheres (MnO@CNSs): A theranostic agent for magnetic resonance imaging-guided photothermal therapy, *Carbon* 136 (2018) 113–124.
- [20] W. Yang, Z.A. Su, Z. Xu, W. Yang, Y. Peng, J. Li, Comparative study of α-, β-, γ- and δ-MnO₂ on toluene oxidation: Oxygen vacancies and reaction intermediates, *Appl. Catal. B-Environ.* 260 (2020), 118150.
- [21] X. Zhou, Q. Liang, B. Yang, Y. Chen, Y. Fang, H. Luo, Y. Liu, Rational design an amorphous multifunctional δ-MnO₂@Fe/Mg-MIL-88B nanocomposites with tailored components for efficient and rapid removal of arsenic in water, *Colloid. Surface. A* 602 (2020), 125141.
- [22] X. Xiao, W. Zhang, H. Zhao, L. Li, P. Deng, Y. Wu, S. Luo, B. Chen, Ultrathin amorphous MnO₂ modified prawn shells-derived porous carbon towards robust oxygen electrocatalyst for rechargeable Zn-air battery, *Angew. Chem.* 13840–13846 (2021).
- [23] H. Bai, S. Liang, T. Wei, Q. Zhou, M. Shi, Z. Jiang, J. Feng, M. Zhang, Z. Fan, Enhanced pseudo-capacitance and rate performance of amorphous MnO₂ for supercapacitor by high Na doping and structural water content, *J. Power. Sources* 523 (2022), 231032.

- [24] J. Hu, H. Wang, F. Dong, Z. Wu, A new strategy for utilization of NIR from solar energy—Promotion effect generated from photothermal effect of $\text{Fe}_3\text{O}_4/\text{SiO}_2$ for photocatalytic oxidation of NO, *Appl. Catal. B-Environ.* 204 (2017) 584–592.
- [25] L. Yang, Y. Xiang, F. Jia, L. Xia, C. Gao, X. Wu, L. Peng, J. Liu, S. Song, Photothermal synergy for boosting photo-Fenton activity with rGO-ZnFe₂O₄: Novel photo-activation process and mechanism toward environment remediation, *Appl. Catal. B-Environ.* 292 (2021), 120198.
- [26] Y. Zheng, W. Wang, D. Jiang, L. Zhang, Amorphous MnOx modified Co₃O₄ for formaldehyde oxidation: improved low-temperature catalytic and photothermocatalytic activity, *Chem. Eng. J.* 284 (2016) 21–27.
- [27] J. Wang, G. Zhang, P. Zhang, Graphene-assisted photothermal effect on promoting catalytic activity of layered MnO₂ for gaseous formaldehyde oxidation, *Appl. Catal. B-Environ.* 239 (2018) 77–85.
- [28] F. Liu, M. Zeng, Y. Li, Y. Yang, M. Mao, X. Zhao, UV-Vis-Infrared light driven thermocatalytic activity of octahedral layered birnessite nanoflowers enhanced by a novel photoactivation, *Adv. Funct. Mater.* 26 (2016) 4518–4526.
- [29] Y. Zeng, J. Zhong, H. Wang, M. Fu, D. Ye, Y. Hu, Synergistic effect of tunable oxygen-vacancy defects and graphene on accelerating the photothermal degradation of methanol over Co₃O₄/rGO nanocomposites, *Chem. Eng. J.* 425 (2021), 131658.
- [30] H. Huang, R. Shi, X. Zhang, J. Zhao, S.U. Chenliang, T. Zhang, Photothermal-assisted triphase photocatalysis over a multifunctional bilayer paper, *Angew. Chem* 42 (2021) 22963–22969.
- [31] L. Li, Z. Huang, Y. Liu, Z. Zhu, M. Xu, W. Wei, Q. Zhang, J. Hong, Novel porous Mn-Fe nanocubes toward peroxymonosulfate activation via non-radical/radical pathways for emerging contaminants degradation, *Appl. Surf. Sci.* 581 (2022), 152390.
- [32] Z. Zhang, H. Ding, Y. Li, J. Yu, L. Ding, Y. Kong, J. Ma, Nitrogen-doped biochar encapsulated Fe/Mn nanoparticles as cost-effective catalysts for heterogeneous activation of peroxymonosulfate towards the degradation of bisphenol-A: Mechanism insight and performance assessment, *Sep. Purif. Technol* 283 (2022), 120136.
- [33] C. Jiao, N. Wei, D. Liu, J. Wang, S. Liu, F. Fu, T. Liu, T. Li, Sustainable Fenton-like degradation of methylene blue over MnO₂-loaded poly(amidoxime-hydroxamic acid) cellulose microrods, *Int. J. Biol. Macromol* 193 (2021) 1952–1961.
- [34] Y.J. Zhang, L. Zhang, L. Kang, M.Y. Yang, K. Zhang, A new CaWO₄/alkali-activated blast furnace slag-based cementitious composite for production of hydrogen, *Int. J. Hydrogen Energ.* 42 (2017) 3690–3697.
- [35] Y.J. Zhang, P.Y. He, Y.X. Zhang, H. Chen, A novel electroconductive graphene/fly ash-based geopolymer composite and its photocatalytic performance, *Chem. Eng. J.* 334 (2018) 2459–2466.
- [36] Y.J. Zhang, P.Y. He, H. Chen, A novel CdO/graphene alkali-activated steel slag nanocomposite for photocatalytic degradation of dye wastewater, *Ferroelectrics* 522 (2018) 1–8.
- [37] X. Zhan, L. Wang, C. Hu, J. Gong, T. Xu, J. Li, L. Yang, J. Bai, S. Zhong, Co-disposal of MSWI fly ash and electrolytic manganese residue based on geopolymeric system, *Waste Manage.* 82 (2018) 62–70.
- [38] Q. Su, S. Yang, Y. He, Z. Qin, X. Cui, Prepared self-growing supported nickel catalyst by recovering Ni (II) from metal wastewater using geopolymer microspheres, *J. Hazard. Mater.* 389 (2020), 121919.
- [39] J. Zhang, Y. Ge, S. Xiong, Z. Li, Catalytic depolymerization of lignin into monophenols over an amorphous mesoporous geopolymer monolith, *J. Clean. Prod.* 332 (2022), 130115.
- [40] X. Cai, Q. Huang, Z. Hong, Y. Zhang, H. Hu, Z. Huang, J. Liang, Y. Qin, Cu anchored on manganese residue through mechanical activation to prepare a Fe-Cu@SiO₂/starch-derived carbon composites with highly stable and active visible light photocatalytic performance, *J. Environ. Chem. Eng.* 9 (2021), 104710.
- [41] X. Cai, Y. Zhang, H. Hu, Z. Huang, Y. Yin, X. Liang, Y. Qin, J. Liang, Valorization of manganese residue to prepare a highly stable and active Fe₃O₄@SiO₂/starch-derived carbon composite for catalytic degradation of dye waste water, *J. Clean. Prod.* 258 (2020), 120741.
- [42] Q. Huang, X. Cai, M. Chen, Q. Yang, S. Fan, Y. Zhang, H. Hu, T. Gan, Z. Huang, A stepwise processing strategy for treating manganese residue and the remediation of hexavalent chromium in water and soil by manganese residue-derived (Fe, Mn)₂C₂O₄, *Chem. Eng. J.* 436 (2022), 135258.
- [43] D. Xia, H. Liu, B. Xu, Y. Wang, Y. Liao, Y. Huang, L. Ye, C. He, P.K. Wong, R. Qiu, Single Ag atom engineered 3D-MnO₂ porous hollow microspheres for rapid photothermocatalytic inactivation of E. coli under solar light, *Appl. Catal. B-Environ.* 245 (2019) 177–189.
- [44] S. Wang, T. He, P. Chen, A. Du, K.K. Ostrikov, W. Huang, L. Wang, In situ formation of oxygen vacancies achieving near-complete charge separation in planar BiVO₄ photoanodes, *Adv. Mater.* 32 (2020) 2001385.
- [45] X. Liu, B. Sui, P.H.C. Camargo, J. Wang, J. Sun, Tuning band gap of MnO₂ nanoflowers by Alkali metal doping for enhanced Ferroptosis/phototherapy synergism in Cancer, *Appl. Mater. Today* 23 (2021), 101027.
- [46] T. Li, J. Liang, L. Zhou, Fabricating Fe₃O₄-schwertmannite as a Z-scheme photocatalyst with excellent photocatalysis-Fenton reaction and recyclability, *J. Environ. Sci.* 186–189 (2020).
- [47] L. Miao, Y. Xie, Y. Xia, N. Zou, J. Wang, Facile photo-driven strategy for the regeneration of a hierarchical C@MnO₂ sponge for the removal of indoor toluene, *Appl. Surf. Sci.* 481 (2019) 404–413.
- [48] Q. Wu, H. Yang, L. Kang, Z. Gao, F. Ren, Fe-based metal-organic frameworks as Fenton-like catalysts for highly efficient degradation of tetracycline hydrochloride over a wide pH range: Acceleration of Fe(II)/ Fe(III) cycle under visible light irradiation, *Appl. Catal. B-Environ.* 263 (2020), 118282.
- [49] H. Dong, X. Zhang, J. Li, P. Zhou, S. Yu, N. Song, C. Liu, G. Che, C. Li, Construction of morphology-controlled nonmetal 2D/3D homojunction towards enhancing photocatalytic activity and mechanism insight, *Appl. Catal. B-Environ.* 263 (2020), 118270.
- [50] J. Xie, L. Chen, X. Luo, L. Huang, S. Li, X. Gong, Degradation of tetracycline hydrochloride through efficient peroxymonosulfate activation by B, N co-doped porous carbon materials derived from metal-organic frameworks: Nonradical pathway mechanism, *Sep. Purif. Technol* 281 (2022), 119887.
- [51] Z. He, M.S. Siddique, H. Yang, Y. Xia, J. Su, B. Tang, L. Wang, L. Kang, Z. Huang, Novel Z-scheme In₂S₃/Bi₂WO₆ core-shell heterojunctions with synergistic enhanced photocatalytic degradation of tetracycline hydrochloride, *J. Clean. Prod.* 339 (2022), 130634.
- [52] W. Zhang, Y. Peng, Y. Yang, L. Zhang, Z. Bian, H. Wang, Bismuth-rich strategy intensifies the molecular oxygen activation and internal electrical field for the photocatalytic degradation of tetracycline hydrochloride, *Chem. Eng. J.* 430 (2022), 132963.